




Orientation-dependent hardness of Mo₃Si studied by cube-corner nanoindentation

Weiguang Yang^{1,*} , Georg Hasemann², Ruth Schwaiger^{1,3}, and Manja Krüger²

¹Institute of Energy and Climate Research, Structure and Function of Materials (IEK-2), Forschungszentrum Jülich GmbH, Leo-Brandt-Str. 1, 52425 Jülich, Germany

²Institute of Materials and Joining Technology, Otto-von-Guericke University Magdeburg, Universitätsplatz 2, 39106 Magdeburg, Germany

³Chair of Energy Engineering Materials, Faculty 5, RWTH Aachen University, 52056 Aachen, Germany

Received: 22 July 2023

Accepted: 19 November 2023

Published online:
19 December 2023

© The Author(s), 2023

ABSTRACT

Mo₃Si crystals having crystallographic out-of-plane orientations close to (001), (011) and (123) were studied by nanoindentation to better understand the hardness anisotropy. The Mo₃Si precipitates were grown in a Mo-17.5Si-6B alloy and identified by electron backscatter diffraction. Pronounced material pile-up around the indents was observed, which causes inaccuracies in the projected contact area determined using the Oliver–Pharr method of around 30% compared to the real one. Based on the analysis of scanning electron micrographs, the projected contact areas and thus the hardness values were determined. To rationalize the observed pronounced orientation dependence of the hardness of Mo₃Si, we suggest an easy-slip-cutting model accounting for the available slip systems as well as the upward flow of material along the surface of the cube-corner indenter tip.

Introduction

With high melting points above 2000 °C, Mo–Si–B alloys show great potential as future high-temperature materials. Their mechanical properties may even exceed the properties of single-crystal nickel-based superalloys and make Mo–Si–B alloys attractive candidates as turbine blade materials [1]. The Mo–Si–B alloys within the Berczik triangle [2], which consists of the molybdenum solid solution (Mo_{ss}) and two intermetallic phases, i.e., Mo₃Si and Mo₅SiB₂, attract the most

attention because they combine the good fracture toughness of Mo_{ss}, the high creep resistance of Mo₃Si and Mo₅SiB₂ and the good oxidation behavior due to the formation of a protective borosilicate layer on the alloy surface [3–7].

The Mo_{ss}–Mo₃Si–Mo₅SiB₂ near-eutectic directionally solidified alloys have outstanding creep resistance [8–10]. Recently, the preferential growth of ⟨001⟩ Mo_{ss} // ⟨001⟩ Mo₃Si // ⟨100⟩ Mo₅SiB₂ along the solidification direction has been reported [11, 12]. Therefore, considering the low fracture toughness and ductility of

Handling Editor: P. Nash.

Address correspondence to E-mail: w.yang@fz-juelich.de

E-mail Addresses: georg1.hasemann@ovgu.de; r.schwaiger@fz-juelich.de; manja.krueger@ovgu.de

the Mo–Si–B alloys at room temperature [1], the investigation of the orientation-dependent plastic deformation behavior of $\text{Mo}_{5\text{ss}}$, Mo_3Si and Mo_5SiB_2 phases at room temperature is of great interest.

Mo has a body-centered cubic (bcc) crystal structure. Due to the non-planar atomic core of screw dislocations in a bcc crystal structure [13–16], the orientation-dependent plastic deformation behavior of Mo at room temperature can be influenced by the tension-compression asymmetry, strain rate and occurrence of anomalous slip [17–20].

Mo_5SiB_2 phase shows a narrow solubility range around the Mo_5SiB_2 stoichiometry [21] and has a body-centered tetragonal crystal structure $D8_1$ [22]. In the unit cell of Mo_5SiB_2 , there are 20 Mo, 4 Si and 8 B atoms. After the investigation on the orientation-dependent plastic deformation behavior of Mo_5SiB_2 at room temperature by performing micropillar compression tests, the critical resolved shear stress was determined for the observed slip systems, i.e., $(001)(100)$, $\{110\}\langle 1\bar{1}0\rangle$ and $\{0\bar{1}1\}\langle 111\rangle$ [23].

Mo_3Si has a narrow solubility range of 23.5–24 at.% Si [24] and exhibits the A15 crystal structure [25]. In the unit cell of the Mo_3Si crystal, the positions of the Si atoms are at the cubic corners and the center, while a Mo–Mo chain can be found on each cubic plane. Mo–Mo chains lie along $\langle 010\rangle$ directions and are orthogonal to one another [26]. The lattice parameter of Mo_3Si is 4.897 Å, and the shortest Mo–Mo distance is 2.449 Å corresponding to nearly half of the lattice parameter [27].

Regarding the orientation-dependent plastic deformation behavior of Mo_3Si at room temperature, the hardness of Mo_3Si single crystals, which was measured by using a Berkovich tip with the maximum load of 20 mN, in (100) , 22.5 ± 0.5 GPa, is almost same as that in (110) , 22.0 ± 0.7 GPa, but 8 % higher than that in (111) [28]. This range of hardness agrees well with the hardness of a Mo_3Si nanocrystalline coating, 23.0 ± 0.5 GPa, which was measured by using a Berkovich tip with the same maximum load (20 mN) [29]. However, it is not consistent with the hardness measured by using a Vickers indenter with the maximum load of 5 N, where a lower range of hardness and a different hardness anisotropy were observed, i.e., hardness in (100) , 14.5 ± 0.1 GPa, is 2 % and 5 % higher than in (111) and (110) , respectively [30]. It could be due to the crack effect at the maximum load of 5 N. The orientation-dependent plastic deformation behavior of the Mo_3Si phase, which is the phase with the

highest volume fraction in the $\text{Mo}_{5\text{ss}}\text{-Mo}_3\text{Si-Mo}_5\text{SiB}_2$ near-eutectic alloys [10, 31], is the focus of the present work.

Knowledge of the slip systems of Mo_3Si helps to understand its orientation-dependent plastic deformation behavior. Based on transmission electron microscopy (TEM), the $\{100\}\langle 010\rangle$ slip systems were reported for Mo_3Si in a $\text{Mo}_3\text{Si-Mo}_5\text{Si}_3\text{-Mo}_5\text{SiB}_2$ sample after 5 % deformation in the temperature range 1240 °C to 1320 °C [32]. The $\{100\}\langle 010\rangle$ slip systems were confirmed in an undeformed as-cast $\text{Mo}_3\text{Si-Mo}_5\text{Si}_3$ alloy [26]. Because of the strong bonding along the Mo–Mo chain, slip along the direction of the chain, i.e., along $\{100\}\langle 001\rangle$, is more difficult than the slip along the direction perpendicular to the chain, i.e., $\{100\}\langle 010\rangle$ [26]. Furthermore, slip along (110) and $\langle 111\rangle$ directions would break the Mo–Mo chains. Thus, $\{100\}\langle 010\rangle$ slip systems are the easiest in Mo_3Si at room temperature [26]. At 1325 °C, not only $\{001\}$ but also $\{012\}$ slip planes were reported [33] based on a slip trace analysis of hot compressed Mo_3Si single crystals. Assuming that the plastic deformation of Mo_3Si obeys Schmid's law at 1325 °C and the difference between the critical shear stresses of different slip systems is small, the hot compression of Mo_3Si single crystals along (111) and (110) revealed critical shear stresses of the $\{100\}\langle 010\rangle$ and $\{012\}\langle 100\rangle$ slip systems with the initial compressive strain rate of 10^{-3} s^{-1} at 1325 °C of 365 MPa and 358 MPa, respectively, which are almost the identical [33].

In this work, we studied the orientation-dependent hardness of the Mo_3Si phase in a Mo–Si–B alloy at room temperature by nanoindentation with a cube-corner tip. Different grain orientations were identified by electron backscatter diffraction and indented inside a scanning electron microscope facilitating precise positioning of the indents. The experimentally determined orientation-dependent hardness will be discussed employing an easy-slip-cutting model with active slip systems identified using Schmid's law.

Experimental details

A 15 g button of the alloy Mo–17.5Si–6B (composition given in at.%) was produced by conventional arc-melting under Ar atmosphere using pure Mo (99.95 wt%), Si (99.999 wt%) and B (99.5 wt%) chips or flakes. To achieve good homogeneity, the button was flipped and re-melted five times. Its chemical composition

was confirmed by inductively coupled plasma optical emission spectroscopy (ICP-OES, iCAP 7600, Thermo Fisher Scientific, USA). Subsequently, a piece of the sample was cut from the button and prepared for electron backscatter diffraction (EBSD) and nanoindentation. After grinding to 2000 grit, the specimen was polished with 15 μm , 6 μm , 3 μm and 1 μm diamond suspensions and finished with 50 nm amorphous colloidal silica suspension.

EBSD (NordlysNano, Oxford Instruments, UK) integrated into a Zeiss Merlin scanning electron microscope (SEM, Zeiss Microscopy, Oberkochen, Germany) was performed with a scan step smaller than 0.65 μm to characterize the crystallographic orientation of the grains in the Mo-Si-B specimen. From the six different

mapping areas (spanning a region of 0.318 mm^2) that were scanned by EBSD, three crystallographic orientations of the Mo_3Si phase, which have the largest misorientations between each other, were selected for testing (Fig. 1). In the further discussion, we will refer to the nominal crystallographic planes identified. The misorientations between the nominal and measured crystallographic planes are summarized in Table 1.

Nanoindentation experiments were conducted using a Hysitron PI 88 SEM PicoIndenter (Bruker, USA) equipped with a diamond cube-corner tip integrated into a Zeiss Merlin SEM (Zeiss Microscopy, Oberkochen, Germany). A preload of 0.1 mN was applied to establish contact between tip and sample. Then, the sample was loaded at a constant indentation

Figure 1 EBSD band contrast images showing the Mo_3Si phase. The crystal orientations close to **a** (001), **b** (011), and **c** (123) are marked in red, green, and blue, respectively. Other orientations of Mo_3Si are shown in white. The scan steps used in (a), (b) and (c) are 0.64 μm , 0.53 μm and 0.37 μm , respectively. **d** Inverse pole figure showing the three crystal orientations selected.

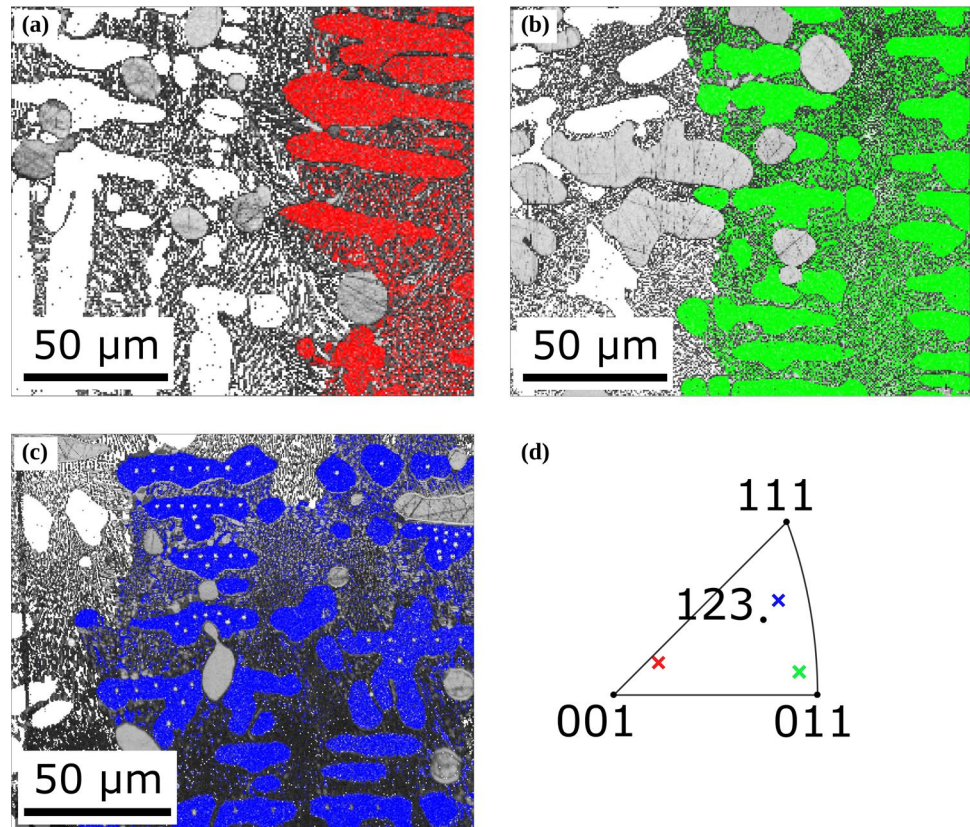


Table 1 Misorientations between the nominal crystallographic orientations and the measured ones based on the Euler angles and the number of indents performed in each measured orientation

Nominal planes (<i>hkl</i>)	Nominal orientations ($\varphi_1, \Phi, \varphi_2$)	Measured orientations ($\varphi_1, \Phi, \varphi_2$)	Misorientations [deg]	Number of indents performed	
				to 5 mN	to 8 mN
(001)	(31°, 0°, 54.1°)	(31°, 11.9°, 54.1°)	11.9	17	6
(011)	(265°, 45°, 0°)	(265°, 41.1°, 7.1°)	6.2	25	10
(123)	(66.6°, 36.7°, 26.6°)	(66.6°, 41.8°, 29.9°)	5.5	36	12

strain rate of 0.05 s^{-1} to the maximum load. Indents to maximum loads of 5 mN and 8 mN were performed, and numbers of the indents are listed in Table 1. The two loads were selected to check the influence of an indentation size effect [34]. As reported by Swadener et al. [28], the hardness of Mo_3Si crystals determined using a Berkovich tip did not show an indentation size effect for depths $> 40 \text{ nm}$ and was almost constant after an initial pop-in. After holding the maximum load for 5 s, the tip was unloaded within 30 s.

The hardness H_{real} was determined based on the evaluation of the projected contact area from SEM micrographs using Eq. (1), where P_{max} is the maximum load and A_{real} is the real projected contact area. Since we needed to exclude inaccuracies in the hardness values due to pile-up or sink-in effects, we did not apply the well-known Oliver–Pharr method [35], but analyzed the micrographs of the residual indents and determined the contact areas using the GNU Image Manipulation Program (GIMP) as exemplified in Fig. 2. SEM micrographs were shown to be

very effective in determining the projected contact area of indents and, subsequently, the hardness of materials [35–40].

To estimate the pile-up effect on the hardness, we also determined the hardness H_{ideal} defined in Eq. (2), where A_{ideal} is the ideal projected area of the residual indent (Fig. 2c). The hardness ratio $F_{\text{pile-up}}$ defined in Eq. (3) then reflects the pile-up effect.

$$H_{\text{real}} = \frac{P_{\text{max}}}{A_{\text{real}}} \quad (1)$$

$$H_{\text{ideal}} = \frac{P_{\text{max}}}{A_{\text{ideal}}} \quad (2)$$

$$F_{\text{pile-up}} = \frac{H_{\text{ideal}} - H_{\text{real}}}{H_{\text{ideal}}} \quad (3)$$

Figure 2 The contact area was determined based on SEM analysis of the indented regions: **a** the indents exhibited significant pile-up resulting in **b** large differences between the real contact area (blue lines) and the ideal one (green lines). **c** Schematic illustration of the real and ideal projected area with pile-up. The real contact area was approximated by the blue lines along the curved edges of the indents as exemplified in (b).

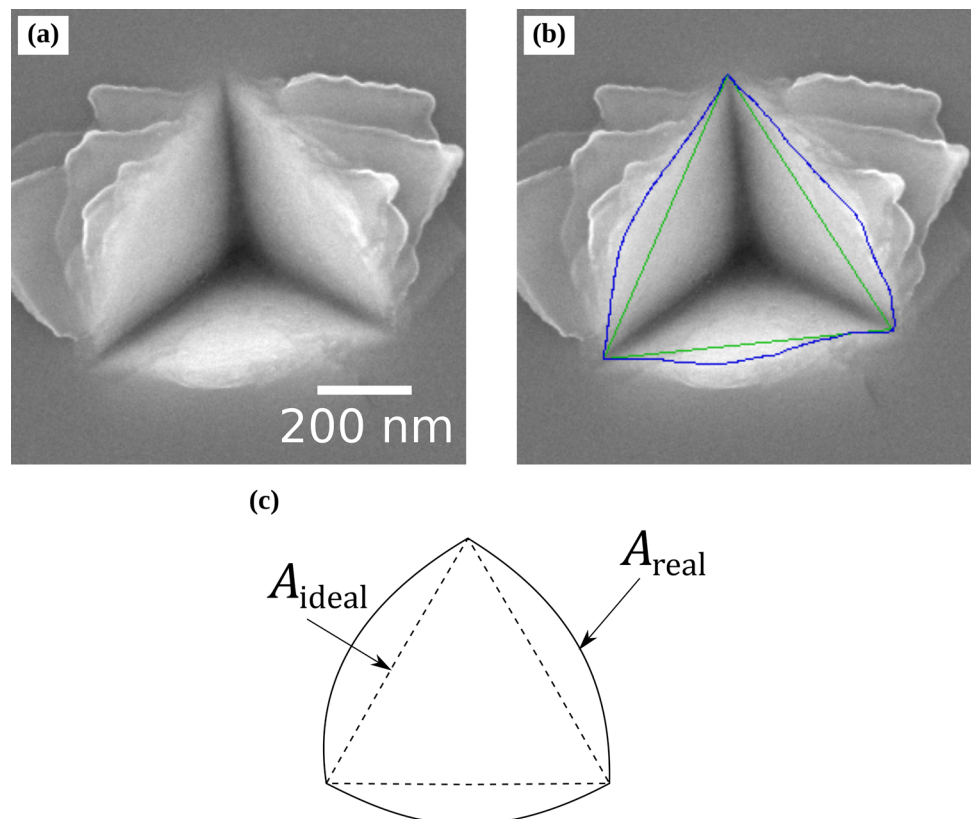
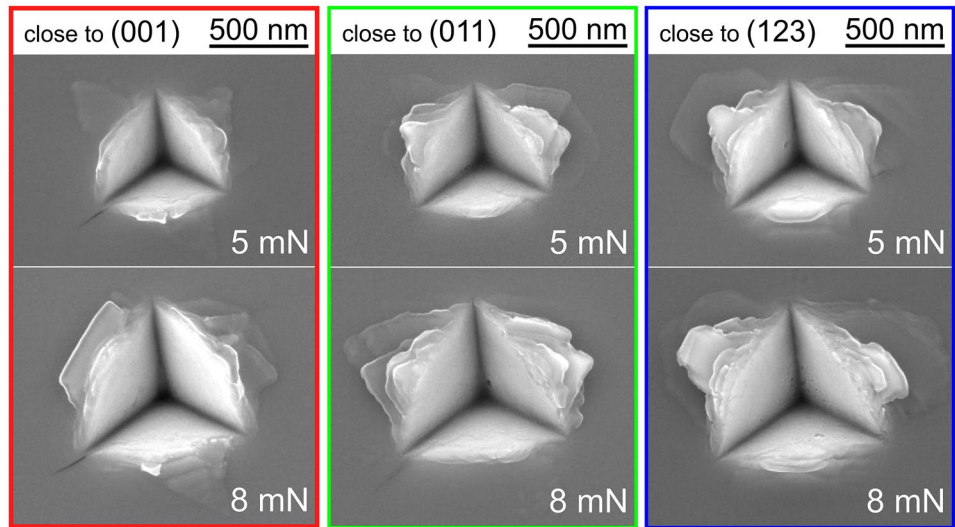


Figure 3 Typical SEM micrographs of indents into Mo₃Si grains with out-of-plane orientations close to (001), (011), and (123). Indentation experiments to two maximum loads of 5 mN and 8 mN were conducted. The material pile-up around the indents appears less pronounced close to (001) for both maximum loads compared to the other two directions.



Results

Indentation with the cube-corner tip caused a significant pile-up in each of the three crystal orientations investigated (Fig. 3). The hardness H_{real} quite clearly shows anisotropic behavior for the maximum load of 5 mN with the highest value close to (001) and decreases by 10 % and 20 % for the orientations close to (011) and (123), respectively (Fig. 4). For 8 mN maximum load, the real hardness close to (001) is the same compared to the lower load, while close to (011) and (123) the hardness values are higher by 5 % and 9 %, respectively (Fig. 4). For both maximum loads, the material pile-up around the indents appeared more pronounced for the orientations close to (011) and (123) than close to (001). However, the effect of the material pile-up evaluated for the indents to 5 mN shows almost no anisotropy, while the pile-up effect for the 8 mN indents is clearly anisotropic (Fig. 4) with an increase of 8 % and 11 % for (011) and (123), respectively, relative to (001).

Discussion

To rationalize the dependence of the hardness of WC and ZrB₂ on the crystallographic orientation, an easy-slip model [41, 42] was suggested assuming the activation of slip systems according to Schmid’s law. The easy-slip model was based on the assumption that the plastic stress field around a Berkovich tip is compressive stress perpendicular to the surface of a conical tip

with the same included half-angle as the axis-to-face angle of a Berkovich tip. This model has been applied to rationalize the orientation-dependent hardness of many hexagonal crystals [41–45], but its application on a cubic crystal has not yet been reported. In the following, we will discuss the observed hardness anisotropy of Mo₃Si based on an extended easy-slip model.

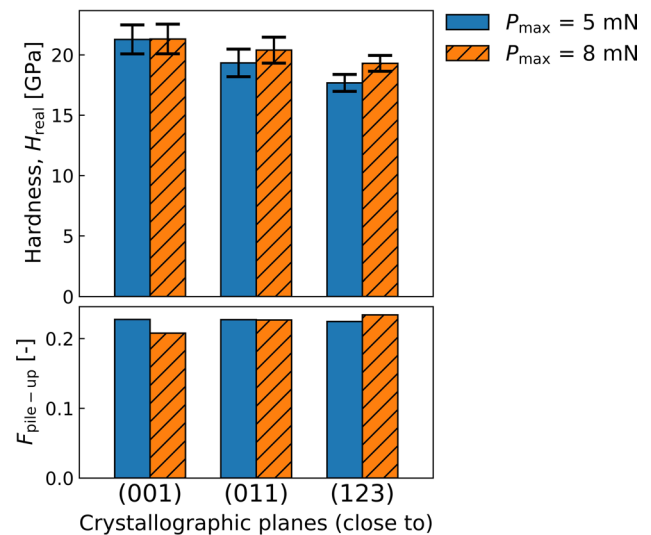


Figure 4 Hardness value H_{real} (see the top chart) and the effect of material pile-up (see the bottom chart) for the three orientations close to (001), (011) and (123). The hardness exhibits anisotropic behavior at both 5 mN and 8 mN, while the pile-up effect reveals clear anisotropic behavior only at the maximum load of 8 mN.

The easy-slip model, however, does not consider the formation of a pile-up around the indent as seen in this study, i.e., the situation of material flow upward along the surface of an indenter tip. Such material flow, though, plays an important role in plastic deformation according to the cutting mechanism [46]. Here, we propose an extension of the easy-slip model to describe the hardness dependence on the crystallographic orientations, which we will describe below. The suggested easy-slip-cutting model can account for the significant material pile-up around indents observed in Mo₃Si.

Easy-slip-cutting model

We base our suggested easy-slip-cutting model on three assumptions: (i) The plastic stress field around a cube-corner tip can be reduced to plane stress, where the maximum shear stress $\tau_{\max,\omega}^*$ is oriented parallel to the surface of the tip (Fig. 5a). The stress is distributed homogeneously around a conical tip with the included half-angle of 35.3°, which is the axis-to-face angle of a cube-corner tip. The corresponding plane stress state is shown at the angle ω between the x -axis and the

projected direction of σ_{ω}^* on the x - y -plane (Fig. 5b). (ii) The plastic deformation around the indent is caused by the slip of dislocations, which distribute homogeneously on each slip plane. The slip of dislocations is activated when the maximum resolved shear stress of a certain slip system reaches the critical resolved shear stress, which is invariable for the same kind of slip system. (iii) Twelve slip systems (Table 2) are considered as potential slip systems for Mo₃Si at room temperature, based on the TEM observation of dislocations in Mo₃Si [26]. Note that assumptions (ii) and (iii) are identical to the ones made in the easy-slip model [41].

According to Hill et al. [47], $|\sigma_{\omega}^*|$, which is the hydrostatic compressive stress, has a linear relation with the maximum shear stress $|\tau_{\max,\omega}^*|$ as reflected in Eq. (4). To simplify the calculation, the stress state is transformed to the principal stress state by anticlockwise rotation of the original stress state by 45° using Mohr's circle as illustrated in Fig. 5c. From this principal stress state, the deviatoric compressive stress state in Fig. 5d can be obtained by eliminating the hydrostatic stress, which does not contribute to plastic deformation.

Figure 5 Schematic illustration of the main assumption of the suggested easy-slip-cutting model: **a** the maximum shear stress $\tau_{\max,\omega}^*$ is oriented parallel to the surface of the tip; **b** plane stress state in the material indented by a cube-corner tip; **c** transformation of the plane stress state using Mohr's circle; **d** transformed deviatoric compressive plane stress state.

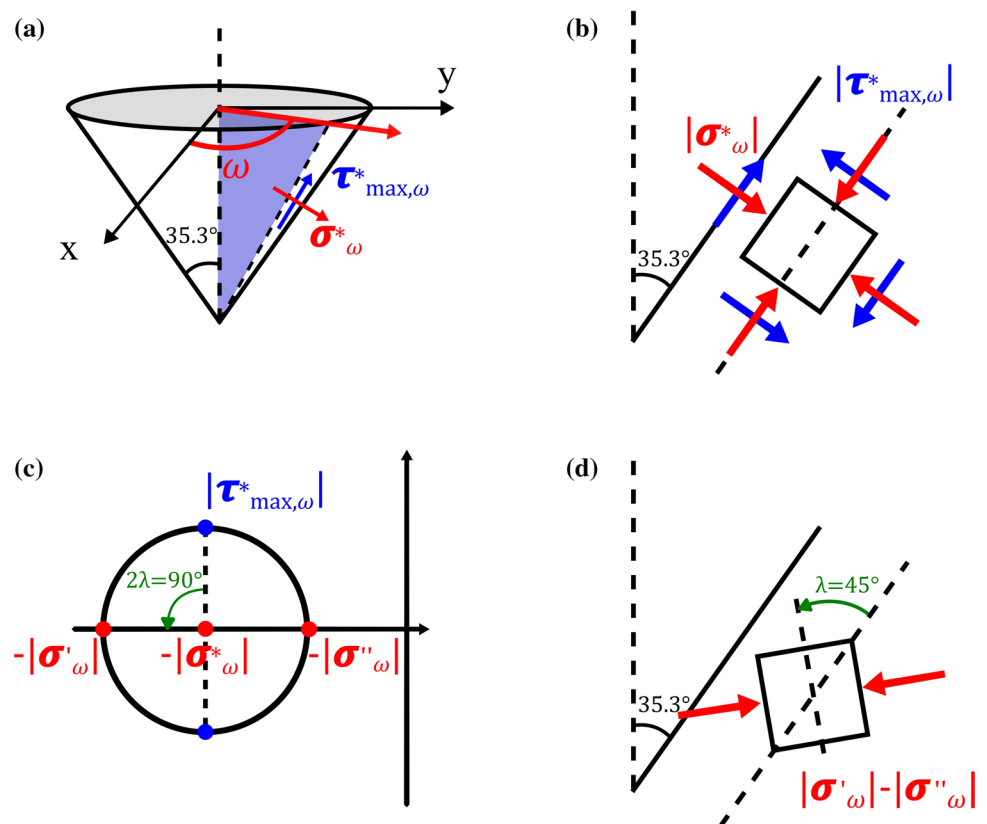


Table 2 Potential slip systems of Mo₃Si at room temperature [26]

<i>i</i>	<i>n_i</i>	<i>v_i</i>	<i>i</i>	<i>n_i</i>	<i>v_i</i>	<i>i</i>	<i>n_i</i>	<i>v_i</i>	<i>i</i>	<i>n_i</i>	<i>v_i</i>
1	(100)	[010]	2	(100)	[0 $\bar{1}$ 0]	3	($\bar{1}$ 00)	[010]	4	($\bar{1}$ 00)	[0 $\bar{1}$ 0]
5	(010)	[001]	6	(010)	[00 $\bar{1}$]	7	(0 $\bar{1}$ 0)	[001]	8	(0 $\bar{1}$ 0)	[00 $\bar{1}$]
9	(001)	[100]	10	(001)	[$\bar{1}$ 00]	11	(00 $\bar{1}$)	[100]	12	(00 $\bar{1}$)	[$\bar{1}$ 00]

A slip system is described in terms of slip plane *n_i*, and slip direction *v_i*, which are given in the form of Miller indices

$$|\sigma_\omega^*| = k|\tau_{\max,\omega}^*| \tag{4}$$

Regardless of the unknown values of *k* and $|\tau_{\max,\omega}^*|$ in Eq. (4), the hardness ratio in different orientations can be calculated as follows. The hardness is calculated based on Eq. (5), where σ^* is the average hydrostatic stress perpendicular to the surface of the indenter tip. The ratio of the projected area *A* and the contact area between the indenter tip and material *A_c* depends mainly on the geometry of the indenter tip; thus, *A/A_c* in Eq. (5) is constant. For a certain crystallographic orientation, the maximum resolved shear stress $|\tau_{\max,\omega}|$ is a function of ω . $|\tau_{\max,\omega}|$ for a given ω can be calculated by selecting the maximum Schmid factor among all potential slip systems using Eq. (6), where α and β are the angles between the slip direction, the slip plane normal and the direction of the deviatoric stress. $|\sigma_\omega^*|$ can be calculated in Eq. (7), which is derived by substituting Eq. (4) into Eq. (6). Applying assumption (ii), the maximum resolved shear stress $|\tau_{\max,\omega}|$ can be replaced by the critical resolved shear stress τ_{crss} in Eq. (8) when dislocation slip is activated. Then, σ^* can be obtained through integration over the maximum Schmid factor around the indenter tip using Eq. (9). Finally, the hardness ratio between two different orientations can be determined in Eq. (10).

$$H = \frac{P}{A} = \frac{\sigma^* A_c}{A} \tag{5}$$

$$|\tau_{\max,\omega}| = f(\omega) = \max[(\cos \alpha \cos \beta)_{i,\omega}] (|\sigma'_\omega| - |\sigma''_\omega|) = 2\max(m_{i,\omega}) |\tau_{\max,\omega}^*| \tag{6}$$

$$|\sigma_\omega^*| = \frac{|\tau_{\max,\omega}|}{2\max(m_{i,\omega})k} \tag{7}$$

$$|\tau_{\max,\omega}| = \tau_{\text{crss}} \Rightarrow |\sigma_\omega^*| = \frac{\tau_{\text{crss}}}{2\max(m_{i,\omega})k} \tag{8}$$

$$\sigma^* = \frac{\tau_{\text{crss}}}{\frac{k}{\pi} \int_0^{2\pi} \max(m_{i,\omega}) d\omega} \tag{9}$$

$$\frac{H_1}{H_2} = \frac{\left(\int_0^{2\pi} \max(m_{i,\omega}) d\omega\right)_2}{\left(\int_0^{2\pi} \max(m_{i,\omega}) d\omega\right)_1} \tag{10}$$

Model evaluation

As a first step, we applied the easy-slip model [41–43] assuming a Berkovich tip and considering the slip systems of Mo₃Si (Table 2). In agreement with the experimental findings of Swadener et al. [28], the easy-slip model predicts a hardness anisotropy, while the hardness decrease for the (011) and (111) crystallographic planes would be higher than observed experimentally (Fig. 6a), where the measured relative hardness values were not corrected for the pile-up effect [28]. Furthermore, we applied the easy-slip model assuming a cube-corner tip. However, the easy-slip model fails to predict the hardness anisotropy measured in this work (Fig. 6b).

The comparison of the data with the easy-slip-cutting model is presented in Fig. 7a and shows good agreement with the change in hardness for the different crystal orientations and both maximum loads of 5 mN and 8 mN. The differences in the hardness at the two different loads could be related to the surrounding material; since we indented Mo₃Si grains embedded in a harder matrix, i.e., Mo₅₅-Mo₃Si-Mo₅SiB₂ eutectics [48] and Mo₃Si-Mo₅SiB₂ eutectics [48] (Fig. 8), there might be a more pronounced contribution of the surrounding material to the hardness of the higher-load indents. However, the use of a cube-corner tip may have a larger effect since the friction between tip and indented material cannot be neglected [49]. Friction would increase when the contact area between indenter face and material increases and would also affect the pile-up forming around an indent [49]. In

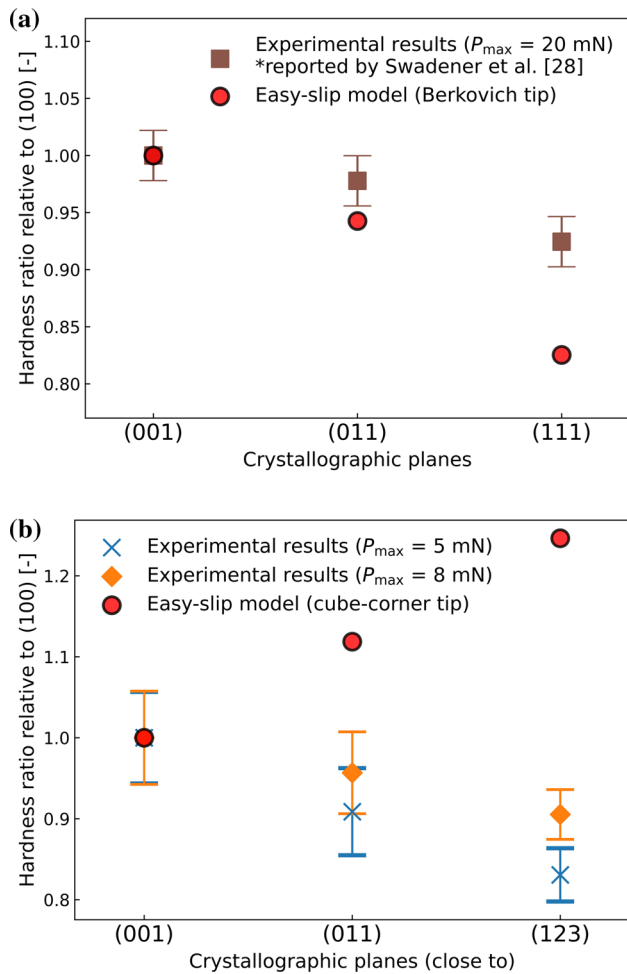


Figure 6 **a** Comparison of the relative hardness change for (001), (011) and (111) crystals based on the experimental hardness reported by Swadener et al. [28] using the Berkovich tip and the relative hardness calculated applying the easy-slip model assuming a Berkovich tip [41–43]. **b** Comparison of the relative hardness measured in this work and that calculated by applying the easy-slip model [41–43] assuming a cube-corner tip.

addition, tip rounding will influence the formation of the plastic zone and has a stronger effect at smaller depths. Furthermore, in the (001) grains, we often observed small cracks for both maximum loads (left panel in Fig. 3), which very likely reduce the hardness values and mask the hardness differences seen for the other grain orientations. The application of the easy-slip-cutting model with the slip systems of Mo_3Si listed in Table 2 is thus promising, and the hardness anisotropy close to (001), (011) and (123) crystallographic planes can be further rationalized by the distribution of the Schmid factor. According to Table 2, seven slip systems will be activated (listed with index

$i = 1, 2, 3, 4, 5, 7, 10$) close to (001), six slip systems ($i = 1, 3, 6, 7, 9, 10$) close to (011), and seven ($i = 1, 2, 3, 6, 7, 10, 11$) close to (123) (Fig. 7b–d). Although the number of activated slip systems for the orientations close to (001), (011) and (123) is comparable, the distribution of the Schmid factor (vs. the rotation angle ω) close to (123) appears more continuous (Fig. 7d), while rather significant minima for the Schmid factor can be observed for the two other crystal orientations, i.e., close to (001) and (011). Thus, the hardness close to the (123) orientation is expected to be the lowest as also observed experimentally. For the crystal orientation close to (001), the main activated slip systems (1–4) have the same or opposite slip plane and slip direction, which results in two pronounced valleys or minima in the Schmid factor graph (Fig. 7b). By contrast, in the distribution of the Schmid factor for the orientation close to (011), one deep valley located between the slip systems 1 and 9 can be seen (Fig. 7c). Therefore, the hardness of the orientation close to (001) should be higher than the one close to (011). The easy-slip-cutting model predicts the orientation dependence of the hardness of Mo_3Si using a cube-corner tip for the different crystallographic orientations (Fig. 9). The crystallographic plane family {001} has the highest hardness, while the family of the {111} planes has the lowest one. As shown in the inverse pole figure of the relative hardness (Fig. 9), the hardness decreases gradually from the corners at {001} to the corners at {111} and {011}.

Summary

The hardness of Mo_3Si , close to crystallographic planes (001), (011) and (123), was investigated by nanoindentation using a cube-corner tip at room temperature. Due to the piled-up material observed around the indents, the hardness was determined based on the evaluation of the projected contact area imaged by SEM. Our findings can be rationalized by applying the easy-slip-cutting model, which is based on the easy-slip model and takes the material pile-up into account, which is caused by the deformation along the surface of the indenter tip and the anisotropy of the potential slip systems of Mo_3Si at room temperature. Our findings are summarized as follows:

1. The experimentally determined hardness values at the maximum loads of 5 mN and 8 mN reveal an

Figure 7 **a** Comparison of experimentally determined hardness anisotropy and the anisotropy based on the easy-slip-cutting model for the three orientations studied. A good agreement between experimental and predicted values can be seen. **b–d** Distributions of the Schmid factor of the potential slip systems (Table 2) around the indent based on the easy-slip-cutting model (close to **(b)** (001), **(c)** (011), **(d)** (123)). The dashed black lines designate the maximum Schmid factor at every ω .

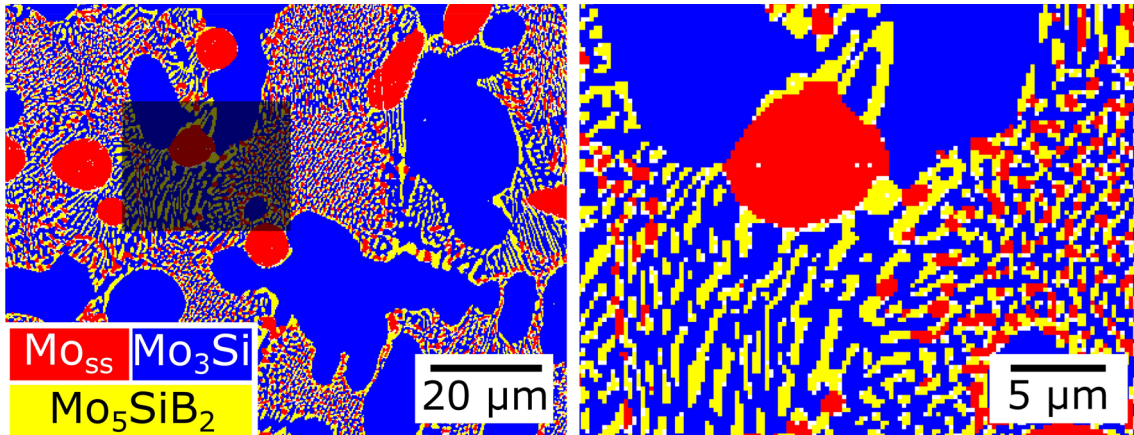
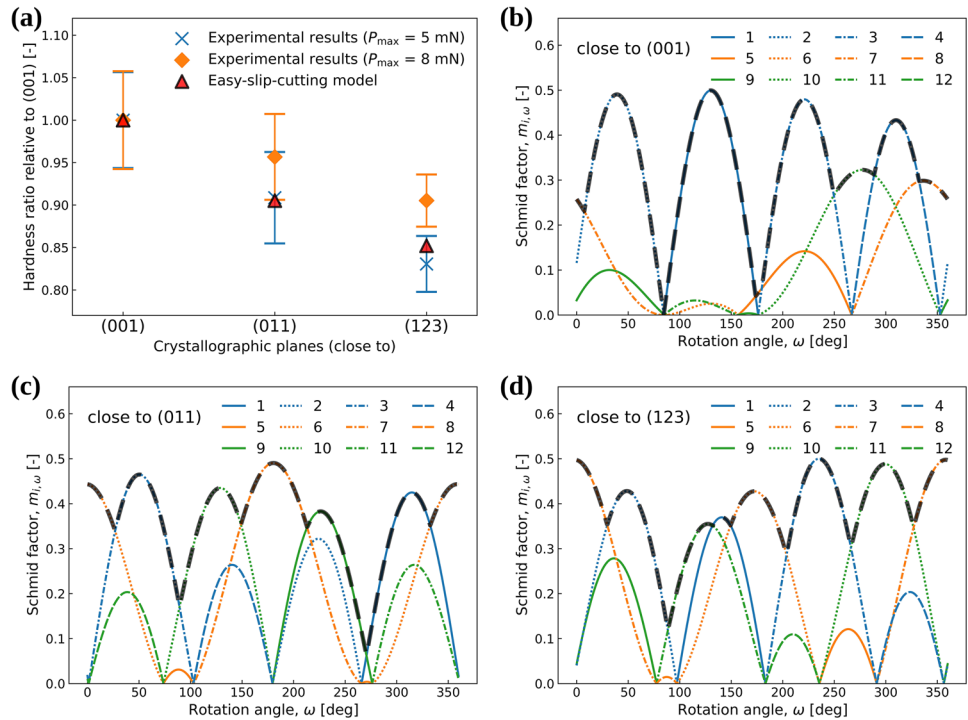


Figure 8 Microstructure (EBSD phase mapping with a scan step of 0.225 μm) of the alloy Mo-17.5Si-6B. The shaded area in the left figure is shown magnified in the right figure. Mo₃Si grains are almost surrounded by the binary and ternary eutectics.

orientation dependence, with the hardness close to (011) being lower than that close to (001) but higher than the hardness close to (123).

2. The hardness values calculated using the easy-slip-cutting model show good agreement with the experimental results. The hardness anisotropy can thus be explained by the distribution of the Schmid factor of the potential slip systems around the indenter tip.

3. Based on the easy-slip-cutting model, we evaluated the hardness anisotropy of Mo₃Si in all crystallographic planes and showed that the hardness of Mo₃Si is highest in {001}, while the lowest value is expected in {111}.

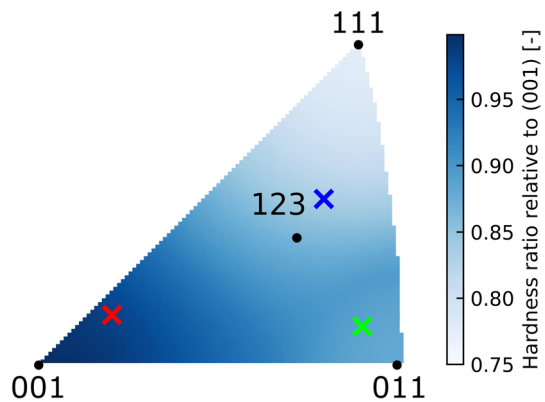


Figure 9 Inverse pole figure of the hardness variation of Mo_3Si with the crystallographic out-of-plane orientations of the Mo_3Si crystals indented in this work (cross symbol). The hardness anisotropy was calculated based on the easy-slip-cutting model assuming a cube-corner tip.

Acknowledgements

This work was supported by the Deutsche Forschungsgemeinschaft (DFG), Germany, project number 410338871. The authors would like to thank Dr. Egbert Wessel (IEK-2, FZ Jülich) for his assistance in the EBSD measurement, SEM investigation and nanoindentation test. Weiguang Yang would like to thank Dr. Jin Wang (IEK-2, FZ Jülich) and Dr. Gang Yan (IAM-AWP, KIT) for the fruitful discussion about Euler angles.

Author contributions

WY was contributed to conceptualization, formal analysis, investigation, methodology, validation, visualization, writing—original draft. GH was contributed to conceptualization, formal analysis, funding acquisition, methodology, supervision, validation, writing—original draft. RS was contributed to conceptualization, formal analysis, funding acquisition, project administration, resources, validation, writing—review and editing. MK was contributed to conceptualization, formal analysis, funding acquisition, project administration, validation, writing—review and editing.

Funding

Open Access funding enabled and organized by Projekt DEAL.

Data and code availability

Data and code will be made available on request.

Declarations

Conflict of interest No potential conflict of interest was reported by the authors.

Ethical approval Not Applicable.

Open Access This article is licensed under a Creative Commons Attribution 4.0 International License, which permits use, sharing, adaptation, distribution and reproduction in any medium or format, as long as you give appropriate credit to the original author(s) and the source, provide a link to the Creative Commons licence, and indicate if changes were made. The images or other third party material in this article are included in the article's Creative Commons licence, unless indicated otherwise in a credit line to the material. If material is not included in the article's Creative Commons licence and your intended use is not permitted by statutory regulation or exceeds the permitted use, you will need to obtain permission directly from the copyright holder. To view a copy of this licence, visit <http://creativecommons.org/licenses/by/4.0/>.

References

- [1] Lemberg JA, Ritchie RO (2012) Mo-Si-B alloys for ultrahigh-temperature structural applications. *Adv Mater* 24(26):3445–3480. <https://doi.org/10.1002/adma.201200764>
- [2] Berczik DM (1997) Method for enhancing the oxidation resistance of a molybdenum alloy, and a method of making a molybdenum alloy. United States Patent (US5595616A)
- [3] Krüger M, Franz S, Saage H et al (2008) Mechanically alloyed Mo-Si-B alloys with a continuous α -Mo matrix and improved mechanical properties. *Intermetallics* 16(7):933–941. <https://doi.org/10.1016/j.intermet.2008.04.015>
- [4] Krüger M, Jain P, Kumar K et al (2014) Correlation between microstructure and properties of fine grained Mo-Mo₃Si-Mo₅SiB₂ alloys. *Intermetallics* 48:10–18. <https://doi.org/10.1016/j.intermet.2013.10.025>
- [5] Kauss O, Obert S, Bogomol I et al (2021) Temperature resistance of Mo_3Si : phase stability, microhardness and

- creep properties. *Metals* 11(4):564. <https://doi.org/10.3390/met11040564>
- [6] Hayashi T, Ito K, Ihara K et al (2004) Creep of single crystalline and polycrystalline T2 phase in the Mo-Si-B system. *Intermetallics* 12(7):699–704. <https://doi.org/10.1016/j.intermet.2004.02.009>
- [7] Rioult FA, Imhoff SD, Sakidja R et al (2009) Transient oxidation of Mo-Si-B alloys: effect of the microstructure size scale. *Acta Mater* 57(15):4600–4613. <https://doi.org/10.1016/j.actamat.2009.06.036>
- [8] Hasemann G, Bogomol I, Schliephake D et al (2014) Microstructure and creep properties of a near-eutectic directionally solidified multiphase Mo-Si-B alloy. *Intermetallics* 48:28–33. <https://doi.org/10.1016/j.intermet.2013.11.022>
- [9] Hasemann G, Kaplunenko D, Bogomol I et al (2016) Near-eutectic ternary Mo-Si-B alloys: microstructures and creep properties. *JOM* 68(11):2847–2853. <https://doi.org/10.1007/s11837-016-2073-0>
- [10] Krüger M, Hasemann G, Kazemi O et al (2017) Microstructure evolution of a directionally solidified ternary eutectic Mo-Si-B alloy. *Mater Sci Forum* 879:1226–1232. <https://doi.org/10.4028/www.scientific.net/MSF.879.1226>
- [11] Zhu L, Ida S, Hasemann G et al (2021) Microstructural characterization of arc-melted and directionally solidified near-eutectic molybdenum-silicon-boron alloys. *Intermetallics* 132:107131. <https://doi.org/10.1016/j.intermet.2021.107131>
- [12] Hasemann G, Zhu L, Hauschildt K et al (2021) In situ observation of ternary eutectic growth in a directionally solidified Mo-Si-B alloy using high-energy synchrotron X-rays. *Adv Eng Mater* 23(11):2100111. <https://doi.org/10.1002/adem.202100111>
- [13] Vitek V (2004) Core structure of screw dislocations in body-centred cubic metals: relation to symmetry and interatomic bonding. *Phil Mag* 84(3):415–428. <https://doi.org/10.1080/14786430310001611644>
- [14] Ito K, Vitek V (2001) Atomistic study of non-schmid effects in the plastic yielding of bcc metals. *Philos Mag A* 81(5):1387–1407. <https://doi.org/10.1080/01418610108214447>
- [15] Woodward C, Rao SI (2001) Ab-initio simulation of isolated screw dislocations in bcc Mo and Ta. *Philos Mag A* 81(5):1305–1316. <https://doi.org/10.1080/01418610108214442>
- [16] Daphalapurkar NP, Patil S, Nguyen T et al (2018) A crystal plasticity model for body-centered cubic molybdenum: experiments and simulations. *Mater Sci Eng A* 738:283–294. <https://doi.org/10.1016/j.msea.2018.09.099>
- [17] Guiu F, Pratt PL (1966) The effect of orientation on the yielding and flow of molybdenum single crystals. *Phys Status Solidi (b)* 15(2):539–552. <https://doi.org/10.1002/pssb.19660150214>
- [18] Lau SS, Dorn JE (1970) Asymmetric slip in Mo single crystals. *Phys Status Solidi (b)* 2(4):825–836. <https://doi.org/10.1002/pssa.19700020420>
- [19] Hsiung LL (2010) On the mechanism of anomalous slip in bcc metals. *Mater Sci Eng A* 528(1):329–337. <https://doi.org/10.1016/j.msea.2010.09.017>
- [20] Gröger R, Chlup Z, Kuběna I et al (2018) Slip activity in molybdenum single crystals compressed at 77 K. *Phil Mag* 98(30):2749–2768. <https://doi.org/10.1080/14786435.2018.1505056>
- [21] Ha SH, Yoshimi K, Maruyama K et al (2012) Compositional regions of single phases at 1800 °C in Mo-rich Mo-Si-B ternary system. *Mater Sci Eng A* 552:179–188. <https://doi.org/10.1016/j.msea.2012.05.028>
- [22] Aronsson B (1958) The crystal structure of Mo₅SiB₂. *Acta Chem Scand* 12:31–37
- [23] Kishida K, Maruyama T, Matsunoshita H et al (2018) Micropillar compression deformation of single crystals of Mo₅SiB₂ with the tetragonal D_{8h} structure. *Acta Mater* 159:416–428. <https://doi.org/10.1016/j.actamat.2018.08.048>
- [24] Rosales I, Schneibel J (2000) Stoichiometry and mechanical properties of Mo₃Si. *Intermetallics* 8(8):885–889. [https://doi.org/10.1016/S0966-9795\(00\)00058-3](https://doi.org/10.1016/S0966-9795(00)00058-3)
- [25] Mitra R (2006) Mechanical behaviour and oxidation resistance of structural silicides. *Int Mater Rev* 51(1):13–64. <https://doi.org/10.1179/174328006X79454>
- [26] Misra A, Petrovic JJ, Mitchell TE (1998) Microstructures and mechanical properties of a Mo₃Si-Mo₅Si₃ composite. *Scripta Mater* 40(2):191–196
- [27] Christensen AN, Stomberg R, Raikas T et al (1983) Preparation and characterization of Mo₃Si and Mo₅Si₃. *Acta Chem Scand* 37a:519–522. <https://doi.org/10.3891/acta.chem.scand.37a-0519>
- [28] Swadener JG, Rosales I, Schneibel JH (2000) Elastic and plastic properties of Mo₃Si measured by nanoindentation. *MRS Online Proc Libr* 646(1):239–244. <https://doi.org/10.1557/PROC-646-N4.2.1>
- [29] Xu J, Hu W, Yan Y et al (2014) Microstructure and mechanical properties of a Mo-toughened Mo₃Si-based in situ nanocomposite. *Vacuum* 109:112–119. <https://doi.org/10.1016/j.vacuum.2014.07.004>
- [30] Rosales I (2008) Synthesis and characterization of Mo₃Si single crystal. *J Cryst Growth* 310(16):3833–3836. <https://doi.org/10.1016/j.jcrysgro.2008.05.044>

- [31] Hasemann G, Krüger M, Palm M et al (2018) Microstructures of ternary eutectic refractory Me-Si-B (Me = Mo, V) alloy systems. *Mater Sci Forum* 941:827–832. <https://doi.org/10.4028/www.scientific.net/MSF.941.827>
- [32] Meyer MK, Kramer MJ, Akinca M (1996) Compressive creep behavior of Mo_5Si_3 with the addition of boron. *Intermetallics* 4(4):273–281. [https://doi.org/10.1016/0966-9795\(95\)00048-8](https://doi.org/10.1016/0966-9795(95)00048-8)
- [33] Rosales I, Schneibel J, Heatherly L et al (2003) High temperature deformation of A15 Mo_3Si single crystals. *Scr Mater* 48(2):185–190. [https://doi.org/10.1016/S1359-6462\(02\)00360-3](https://doi.org/10.1016/S1359-6462(02)00360-3)
- [34] Nix WD, Gao H (1998) Indentation size effects in crystalline materials: a law for strain gradient plasticity. *J Mech Phys Solids* 46(3):411–425. [https://doi.org/10.1016/S0022-5096\(97\)00086-0](https://doi.org/10.1016/S0022-5096(97)00086-0)
- [35] Oliver WC, Pharr GM (2004) Measurement of hardness and elastic modulus by instrumented indentation: advances in understanding and refinements to methodology. *J Mater Res* 19(1):3–20
- [36] Oliver W, Pharr G (1992) An improved technique for determining hardness and elastic modulus using load and displacement sensing indentation experiments. *J Mater Res* 7(06):1564–1583. <https://doi.org/10.1557/JMR.1992.1564>
- [37] Ghisleni R, Rzepiejewska-Malyska K, Philippe L et al (2009) In situ SEM indentation experiments: instruments, methodology, and applications. *Microsc Res Tech* 72(3):242–249. <https://doi.org/10.1002/jemt.20677>
- [38] Sullivan M, Prorok BC (2015) Evaluating indent pile-up with metallic films on ceramic-like substrates. *J Mater Res* 30(13):2046–2054. <https://doi.org/10.1557/jmr.2015.167>
- [39] Hardie CD, Roberts SG, Bushby AJ (2015) Understanding the effects of ion irradiation using nanoindentation techniques. *J Nucl Mater* 462:391–401. <https://doi.org/10.1016/j.jnucmat.2014.11.066>
- [40] Brinckmann S, Schwaiger R (2021) Towards enhanced nanoindentation by image recognition. *J Mater Res* 36(11):2266–2276. <https://doi.org/10.1557/s43578-021-00173-x>
- [41] Csanádi T, Blánda M, Chinh NQ et al (2015) Orientation-dependent hardness and nanoindentation-induced deformation mechanisms of WC crystals. *Acta Mater* 83:397–407. <https://doi.org/10.1016/j.actamat.2014.09.048>
- [42] Csanádi T, Kovalčíková A, Dusza J et al (2017) Slip activation controlled nanohardness anisotropy of ZrB_2 ceramic grains. *Acta Mater* 140:452–464. <https://doi.org/10.1016/j.actamat.2017.08.061>
- [43] Csanádi T, Németh D, Dusza J et al (2016) Nanoindentation induced deformation anisotropy in $\beta\text{-Si}_3\text{N}_4$ ceramic crystals. *J Eur Ceram Soc* 36(12):3059–3066. <https://doi.org/10.1016/j.jeurceramsoc.2015.11.028>
- [44] Yan G, Yu S, Yang W et al (2019) Anisotropy of the mechanical properties of $\text{Li}_{1.3}\text{Al}_{0.3}\text{Ti}_{1.7}(\text{PO}_4)_3$ solid electrolyte material. *J Power* 437:226940. <https://doi.org/10.1016/j.jpowsour.2019.226940>
- [45] Li X, Malzbender J, Yan G et al (2021) A combined experimental and modeling study revealing the anisotropic mechanical response of Ti_2AlN MAX phase. *J Eur Ceram Soc* 41(12):5872–5881. <https://doi.org/10.1016/j.jeurceramsoc.2021.05.015>
- [46] Fischer-Cripps AC (2011) Nanoindentation testing. In: *Nanoindentation*. Mechanical Engineering Series 1, Springer New York, New York, NY, p 11–14. https://doi.org/10.1007/978-1-4419-9872-9_1
- [47] Hill R, Lee EH, Tupper SJ (1947) The theory of wedge indentation of ductile materials. *Proc R Soc Lond A* 188(1013):273–289. <https://doi.org/10.1098/rspa.1947.0009>
- [48] Hasemann G (2017) *Microstructure and properties of near-eutectic Mo-Si-B alloys for high temperature applications*. Shaker Verlag, Aachen
- [49] Wang Y (2016) Effects of indenter angle and friction on the mechanical properties of film materials. *Results in Physics* 6:509–514. <https://doi.org/10.1016/j.rinp.2016.08.008>

Publisher's Note Springer Nature remains neutral with regard to jurisdictional claims in published maps and institutional affiliations.